inorganics

MDPI

Article

Structural Evolution and Hydrogen Sorption Properties of $Y_xNi_{2-y}Mn_y$ ($0.825 \leq x \leq 0.95$, $0.1 \leq y \leq 0.3$) Laves Phase Compounds

Hao Shen [1,2,3], Valerie Paul-Boncour [1], Ping Li [2], Lijun Jiang [3,*] and Junxian Zhang [1,*]

[1] Univ. Paris Est Creteil, CNRS, ICMPE, UMR 7182, 2 Rue Henri Dunant, 94320 Thiais, France
[2] Institute for Advanced Materials and Technology, University of Science and Technology, Beijing 100083, China
[3] National Engineering Research Center of Nonferrous Metals Materials and Products for New Energy, GRINM Group Co., Ltd., Beijing 100088, China
* Correspondence: jlj@grinm.com (L.J.); junxian.zhang@cnrs.fr (J.Z.)

Abstract: The $Y_xNi_{2-y}Mn_y$ system was investigated in the region $0.825 \leq x \leq 0.95$, $0.1 \leq y \leq 0.3$. The alloys were synthesized by induction melting and corresponding annealing. The substitution of Mn for Ni (y = 0.1) favors the formation of a *C*15 structure with disordered Y vacancies against the superstructure of $Y_{0.95}Ni_2$. For y = 0.2 and 0.3, Mn can substitute in both Y and Ni sites. Single-phase compounds with a *C*15 structure can be formed by adjusting both the Y and Mn contents. Their hydrogen absorption–desorption properties were measured by pressure–composition isotherm (PCI) measurements at 150 °C, and the hydrides were characterized at room temperature by X-ray diffraction and TG–DSC experiments. The PCIs show two plateaus corresponding to the formation of crystalline and amorphous hydrides. The heating of the amorphous hydrides leads to an endothermic desorption at first and then a recrystallization into Y(Ni, Mn)$_3$ and YH_x phases. At higher temperatures, the Y hydride desorbs, and a recombination into a Y(Ni, Mn)$_2$ Laves phase compound is observed. For y = 0.1, vacancy formation in the Y site and partial Mn substitution in the Ni site enhance the structural stability and suppress the hydrogen-induced amorphization (HIA). However, for a larger Mn content ($y \geq 0.2$), Mn substitutes also in the Y sites at the expense of Y vacancies. This yields worse structural stability upon hydrogenation than for y = 0.1, as the mean ratio $r_{(Y,\,Mn)}/r_{(Ni/Mn)}$ becomes larger than for y = 0.1 $r_{(Y,\,\square)}/r_{(Ni/Mn)}$.

Keywords: Y-based alloys; Mn substitution; structural properties; hydrogen-induced amorphization

check for updates

Citation: Shen, H.; Paul-Boncour, V.; Li, P.; Jiang, L.; Zhang, J. Structural Evolution and Hydrogen Sorption Properties of $Y_xNi_{2-y}Mn_y$ ($0.825 \leq x \leq 0.95$, $0.1 \leq y \leq 0.3$) Laves Phase Compounds. *Inorganics* **2024**, *12*, 55. https://doi.org/10.3390/inorganics12020055

Academic Editors: Rainer Niewa, Torben R. Jensen, Richard Dronskowski, Christian M. Julien, Guido Kickelbick, Alexander S. Novikov, Gary Hix and Hans-Conrad zur Loye

Received: 24 November 2023
Revised: 19 January 2024
Accepted: 4 February 2024
Published: 7 February 2024

1. Introduction

Hydride-forming AB_n-type alloys (A = rare earth, B = transition metal) are widely used for hydrogen storage [1], as well as negative electrode materials for nickel–metal hydride (Ni–*M*H) batteries [2]. Recently, (A, Mg)Ni-based AB_n alloys ($3 \leq n \leq 4$) with stacking structures have been developed for hydrogen storage [3,4], with the capacity increasing from 1.5 wt.% for AB_5-type alloys to 1.8 wt.% for AB_n ($3 \leq n \leq 4$)-type alloys [5–8]. AB_2-type alloys with a *C*15 Laves phase structure possess more tetrahedral sites than AB_5 and AB_n alloys ($3 \leq n \leq 4$) to accommodate hydrogen atoms; thus, a higher hydrogen absorption capacity is foreseen [9].

Laves phases belong to the class of Frank–Kasper phases showing topologically close-packed structures. The closest packing of hard spheres can be obtained in *C*15 AB_2 alloys, where the A and B atoms show an ideal radius ratio r_A/r_B = 1.225. Hydrogen storage in AB_2 Laves phase compounds has been investigated and is still a hot research subject as it presents a larger hydrogen capacity compared with AB_5 and bcc compounds. Many studies have been performed on ZrB_2 compounds (B = V, Cr, Mn, Fe, Co), whose thermodynamic properties can be adjusted by chemical substitution and which can absorb up to 2 wt.% of hydrogen [10–15]. YB_2 hydrides (B = Mn, Fe, Co, Ni) were also widely studied for

their hydrogenation properties [16,17]. However, depending on the transition metal and the hydrogenation conditions, they can form either crystalline or amorphous hydrides. Disproportionation into transition metal and Y hydride can also occur. In a recent review, all the criteria concerning the AB_2 hydride stability were investigated, and it appears that one critical geometric factor is the r_A/r_B ratio, where r_A and r_B are the atomic radii of the A and B elements, respectively [18]. When this ratio becomes larger than 1.37, hydrogen-induced amorphization (HIA) is favored at the detriment of the hydrogen sorption reversibility. To reduce this ratio towards the ideal ratio r_A/r_B = 1.225 for topologically close-packed structures, it is necessary to either decrease r_A, increase r_B, or play on both elements by appropriate substitutions. Several studies have already been performed on the role of chemical substitutions in the hydrogenation properties of $Y_{0.95}Ni_2$. As Y has a smaller weight than lanthanides, higher weight capacities are expected. $Y_{0.95}Ni_2$ crystallizes in a superstructure with a doubling of the cubic lattice parameter a and a lower symmetric space group $F\bar{4}3m$ (No. 216) compared with the cubic Laves phase ($Fd\bar{3}m$ space group). The superstructure is related to the formation of ordered Y vacancies in the 4a sites and has also been observed in other ANi$_2$ compounds [19,20]. Hydrogen absorption in $Y_{0.95}Ni_2$ yields a crystalline hydride up to 2.7 H/f.u. with the same superstructure type as the parent compound, whereas hydrogen-induced amorphization (HIA) occurs for a larger H content [19,21,22]. The substitution of Y by Sc, which is isoelectronic and has a smaller size than Y, allowed for the reduction of r_A, and HIA was fully eliminated in the $Y_{0.25}Sc_{0.7}Ni_2$ compound [23]. On the other hand, the influence of Al for Ni substitution in $Y_{0.95}Ni_2$ was investigated [21], and for an appropriate Al content, the reversibility was improved.

Another possibility to increase r_B is to substitute Ni by a larger Mn atom. Among various YB_2 compounds, YMn_2 is a $C15$ Laves phase adopting the cubic $MgCu_2$-type structure (space group $Fd\bar{3}m$, No. 227). At room temperature, the YMn_2 hydride remains cubic up to 3.5 H/f.u. and undergoes rhombohedral distortion for a larger H content with a progressive cell volume increase [24]. Upon cooling, various structural distortions are observed, depending on the H content [16,25]. For a hydrogen pressure above 0.5 GPa, a complex YMn_2H_6 hydride, with a fluorite-type structure similar to that of Mg_2FeH_6, is obtained. This structure is different from that of the parent compound with two different sites for the Mn atoms, one sharing the same position as the Y atom, with a disordered substitution, and the other one forming MnH_6 octahedra [26,27]. Furthermore, a recent work by machine learning shows that Mn contributes to increasing the hydrogen storage capacity of AB_2 compounds [28].

In a recent study [29], the structural properties of $Y_xNi_{2-y}Mn_y$ intermetallic compounds were investigated by both experimental work (X-ray and neutron diffraction) and theoretical DFT calculations in order to determine the homogeneity range of Laves phase compounds. It was observed that the rate of Y vacancies varies with the Mn content and that Mn can substitute not only on the Ni but also in the Y site.

This previous work has been completed by the synthesis and characterization of new $Y_xNi_{2-y}Mn_y$ compounds ($y \leq 0.3$), and will be detailed in the first section of this paper.

In addition, the hydrogenation properties of the selected $Y_xNi_{2-y}Mn_y$ ($0.825 \leq x \leq 0.95$, $0.1 \leq y \leq 0.3$) sample forming single-phase compounds have been investigated. Their thermodynamic and structural properties have been studied by measuring pressure–composition isotherms (PCIs), X-ray diffraction patterns, and thermal properties. The influence of the Mn substitution on the metal hydride stability, from both thermodynamic and crystallographic points of view, will be presented and discussed.

2. Results

2.1. Structural Characteristics of $Y_xNi_{2-y}Mn_y$ Compounds

The $Y_{0.95}Ni_2$ compound crystallizes in a single $TmNi_2$-type superstructure type with a doubling of the cubic cell parameter and vacancies in the Y site (space group $F\bar{4}3m$, No. 216) [29–31]. The $Y_{0.9}Ni_{2-y}Mn_y$ ($0.1 \leq y \leq 0.3$) alloys contain Y(Ni, Mn)$_2$ with a $C15$ structure (space group $Fd\bar{3}m$, No. 227) as the main phase, as previously observed for

Al-substituted AB_2 compounds [21]. YNi (*AB*-type, space group *Pnma*, No. 62) appears as a secondary phase, and its abundance increases proportionally with the Mn content. The compounds with $y = 0.4$ and 0.5 contain Y(Ni, Mn)$_3$ (AB_3-type, space group $R\bar{3}m$, No. 166) as the main phase, whose abundance increases at the expense of the AB_2-type one, and will not be treated in the present paper. Single *C*15 Laves phases were obtained for $Y_{0.9}Ni_{1.9}Mn_{0.1}$, $Y_{0.86}Ni_{1.8}Mn_{0.2}$, and $Y_{0.825}Ni_{1.7}Mn_{0.3}$ compounds. In the previous work, neutron diffraction analysis and DFT calculation showed that, at a low Mn content, $Y_xNi_{2-y}Mn_y$ ($x = 0.95$, 0.90, 0.86, 0.825, $y = 0$, 0.1, 0.2, 0.3, 0.4, 0.5), the *C*15 structure is stabilized by vacancies in the *A* site. Meanwhile, for a larger Mn content, stabilization occurs through Mn substitution for Y in the *A* site and a reduction of Y vacancies [30]. The phase abundances and the lattice parameters of $Y_xNi_{2-y}Mn_y$ ($0.825 \leq x \leq 0.95$, $0.1 \leq y \leq 0.3$) obtained by XRD Rietveld analyses are gathered in Table 1. Note that the traces of Y_2O_3 found in the alloys can be either still present in the initial Y ingot, despite surface cleaning, or due to the oxidation of unreacted Y upon thermal treatment.

Table 1. Phase compositions determined by electron probe microanalysis (EPMA) and crystallographic data from Rietveld analyses of $Y_xNi_{2-y}Mn_y$ ($0.825 \leq x \leq 0.95$, $0.1 \leq y \leq 0.3$) compounds; * stands for the data that are published in reference [30].

Sample	Phase	Space Group	Phase Composition (EPMA) (±0.01)	Abundance (wt.%)	Lattice Parameters (Å)		
					a	*b*	*c*
$Y_{0.95}Ni_2$	$Y_{0.95}Ni_2$	$F\bar{4}3m$	$Y_{0.93}Ni_2$	99 (1)	14.3557 (1)	-	-
$Y_{0.9}Ni_{1.9}Mn_{0.1}$ *	Y_{1-v}(Ni, Mn)$_2$	$Fd\bar{3}m$	$Y_{0.86}Ni_{1.87}Mn_{0.13}$	96 (1)	7.1733 (1)	-	-
	Y_2O_3	$Ia\bar{3}$	-	4 (1)	-	-	-
$Y_{0.9}Ni_{1.8}Mn_{0.2}$	Y_{1-v}(Ni, Mn)$_2$	$Fd\bar{3}m$	$Y_{0.87}Ni_{1.79}Mn_{0.21}$	95 (1)	7.1900 (1)	-	-
	YNi	*Pnma*	-	4 (1)	7.131 (2)	4.1505 (1)	5.4858 (1)
	Y_2O_3	$Ia\bar{3}$	-	trace	-	-	-
$Y_{0.9}Ni_{1.7}Mn_{0.3}$	Y_{1-v}(Ni, Mn)$_2$	$Fd\bar{3}m$	$Y_{0.83}Ni_{1.68}Mn_{0.32}$	90 (1)	7.1951 (1)	-	-
	YNi	*Pnma*	$YNi_{0.99}Mn_{0.02}$	9 (1)	7.134 (2)	4.1389 (1)	5.5064 (1)
	Y_2O_3	$Ia\bar{3}$	-	trace	-	-	-
$Y_{0.86}Ni_{1.8}Mn_{0.2}$ *	Y_{1-v}(Ni, Mn)$_2$	$Fd\bar{3}m$	$Y_{0.85}Ni_{1.79}Mn_{0.21}$	99 (1)	7.1826 (1)		-
	Y_2O_3	-	-	trace	-		
$Y_{0.825}Ni_{1.7}Mn_{0.3}$ *	Y_{1-v}(Ni, Mn)$_2$	$Fd\bar{3}m$	$Y_{0.82}Ni_{1.69}Mn_{0.31}$	99 (1)	7.1912 (1)		
	Y_2O_3	-	-	trace		-	

2.2. Hydrogen Sorption Properties

2.2.1. Pressure–Composition Isotherms

After activation pretreatment at 150 °C under vacuum, the PCIs were measured at 150 °C for all $Y_xNi_{2-y}Mn_y$ ($0.825 \leq x \leq 0.95$, $0 \leq y \leq 0.3$) alloys. As shown in Figure 1a, for $Y_{0.9}Ni_{2-y}Mn_y$ ($y = 0.1$, 0.2, 0.3) compounds, the hydrogen storage capacity of the Mn0.1 ($y = 0.1$) compound is about 3.3 H/f.u., slightly lower than 3.8 H/f.u. for Mn0.2 ($y = 0.2$) and Mn0.3 ($y = 0.3$). YNi absorbs hydrogen at room temperature (RT) and forms very stable $YNiH_3$ hydrides [21,32]. The small amount of YNi in the Mn0.2 and Mn0.3 alloys should be responsible for the gap of the first measurable point from zero capacity. All the absorption PCI curves present a first plateau between 0.25 and 1.2 H/f.u., with a relatively flat plateau around a pressure of 5 kPa, and a second sloping plateau between 2.0 and 2.5 H/f.u., with a significant reduction in the plateau pressure with an increasing Mn content (from 0.3 MPa for the Mn0.2 compound to 0.08 MPa for the Mn0.3 compound at hydrogen concentrations of around 2.5 H/f.u.).

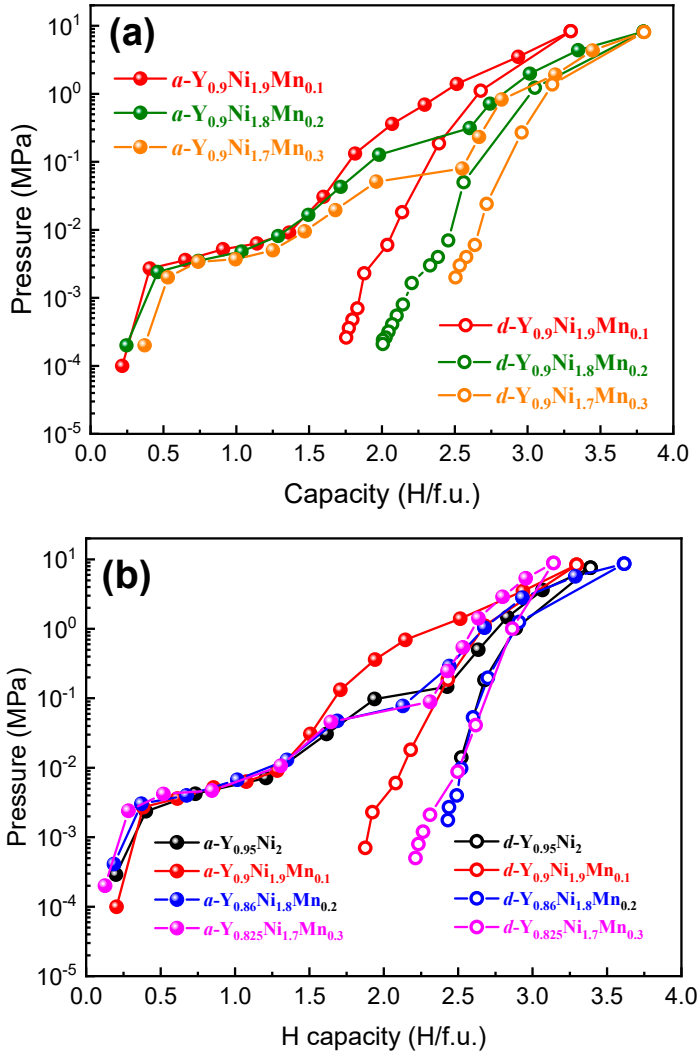

Figure 1. *P–C* isotherms measured at 150 °C for $Y_{0.9}Ni_{2-y}Mn_y$ (y = 0.1, 0.2, 0.3) (**a**) and $Y_xNi_{2-y}Mn_y$ samples with a single superstructure or *C*15 Laves phase structure (**b**); full symbols stand for absorption, and empty symbols stand for desorption; "*a*-" stands for hydrogen absorption, and "*d*-" stands for hydrogen desorption.

A similar behavior has been observed for the single-phase compounds with a superstructure (y = 0) and a single *C*15 structure (Mn-containing compounds) (Figure 1b). The first plateaus overlap each other, showing an equilibrium pressure of 0.005 MPa. In addition, a second plateau can be observed for the $Y_{0.95}Ni_2$, $Y_{0.86}Ni_{1.8}Mn_{0.2}$, and $Y_{0.825}Ni_{1.7}Mn_{0.3}$ compounds, and the Mn for Ni substitution slightly lowers the second plateau pressure. $Y_{0.9}Ni_{1.9}Mn_{0.1}$ shows different behaviors compared with others as a sloped branch is observed between 1.5 and 2.5 H/f.u. Due to the limit of low-pressure measurements, full desorption at 150 °C cannot be achieved.

2.2.2. X-ray Diffraction Results after Hydrogenation

XRD measurements have been performed on $Y_{0.9}Ni_{2-y}Mn_y$ (y = 0.1, 0.2, 0.3) hydrides hydrogenated at room temperature up to various hydrogen concentrations, with a final pressure below 0.1 MPa. The XRD patterns of their hydrides are shown in Figure 2. The crystallographic results obtained from Rietveld refinement for Mn0.1 compounds are summarized in Table 2. For Mn0.2 and Mn0.3 compounds due to the broadness of the diffraction peaks and significant background bumping, Rietveld analyses could not be performed.

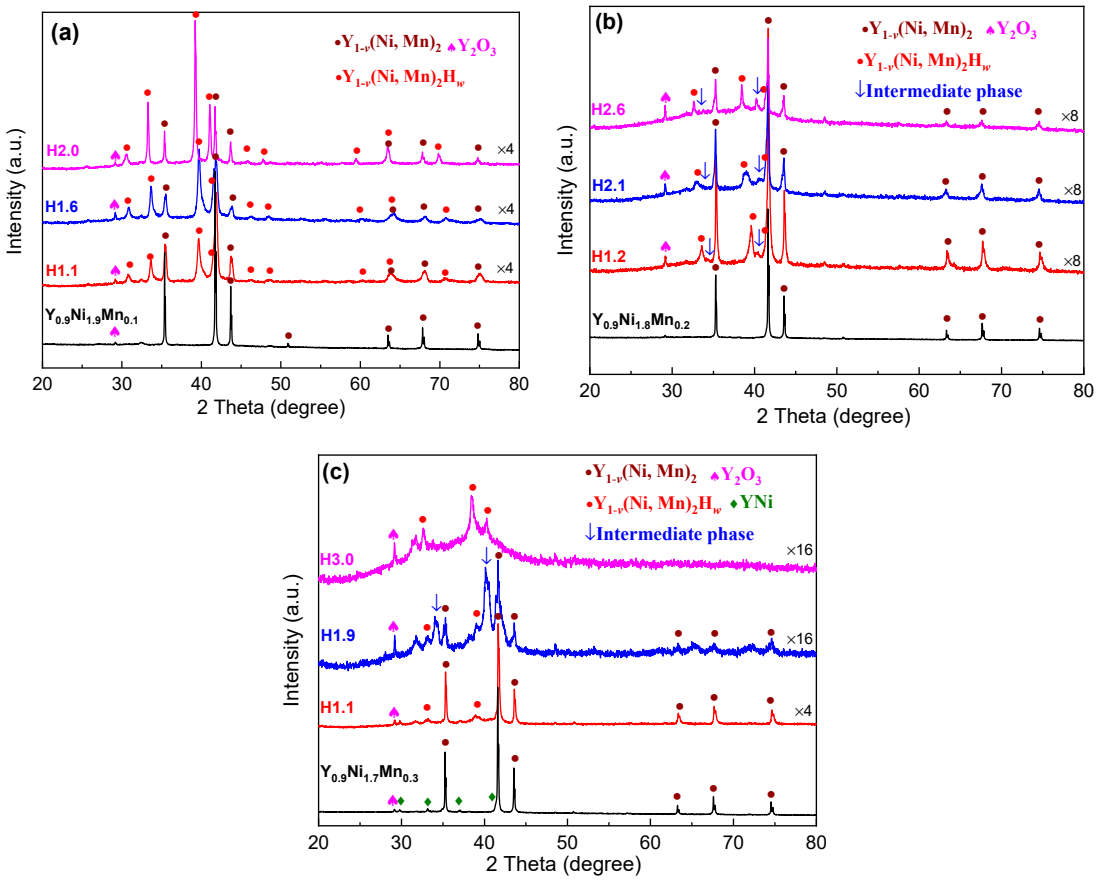

Figure 2. XRD patterns of the hydrides of $Y_{0.9}Ni_{1.9}Mn_{0.1}$ (**a**), $Y_{0.9}Ni_{1.8}Mn_{0.2}$ (**b**), and $Y_{0.9}Ni_{1.7}Mn_{0.3}$ (**c**) with different hydrogen concentrations prepared at room temperature.

Table 2. Crystallographic data of the $Y_{0.9}Ni_{1.9}Mn_{0.1}$ alloy and its hydrides.

Hydrogen Content(H/f.u.)	Phase	Abundance (wt.%)	Space Group	Lattice Parameters(Å)	Cell Volume*V* (Å^3)	Δ*V*/*V*(%)
0	$Y_{1-v}(Ni, Mn)_2$	96 (1)	$Fd\bar{3}m$	7.1733 (1) /14.3466 (2)	369.11 (1) /2952.8 (1)	
	Y_2O_3	4 (1)				
1.1	$Y_{1-v}(Ni, Mn)_2$	47 (1)	$F\bar{4}3m$	14.318 (1)	2935.3 (5)	15.8
	$Y_{1-v}(Ni, Mn)_2H_w$	52 (1)	$F\bar{4}3m$	15.065 (1)	3419.3 (7)	
	Y_2O_3	trace				
1.6	$Y_{1-v}(Ni, Mn)_2$	35 (1)	$F\bar{4}3m$	14.320 (2)	2936.7 (7)	15.5
	$Y_{1-v}(Ni, Mn)_2H_{w'}$	64 (1)	$F\bar{4}3m$	15.051 (2)	3409.7 (9)	
	Y_2O_3	trace				
2.0	$Y_{1-v}(Ni, Mn)_2$	21 (1)	$F\bar{4}3m$	14.357 (1)	2959.4 (4)	19.6
	$Y_{1-v}(Ni, Mn)_2H_{w''}$	78 (1)	$F\bar{4}3m$	15.229 (1)	3532.5 (5)	
	Y_2O_3	trace				

For Mn0.1, up to 2.0 H/f.u., the sample contains two phases crystallizing in the $TmNi_2$ structure, the intermetallic and its corresponding hydride with an expanded lattice parameter. For the two samples with hydrogen contents of 1.2 and 1.6 H/f.u., respectively, the lattice parameter of the hydride remains almost constant, and the fraction of the hydride phase increases. This means that these compounds are located in the two-phase region that corresponds to the first plateau (see PCI at 150 °C in Figure 1a). Between 1.6 and 2.0 H/f.u., the lattice parameter of the hydride phase increases from 15.051 (1) Å to 15.229 (1) Å, and the corresponding cell volume increases from 2952.8 (1) Å^3 to 3532.5 (5) Å^3 (with a

cell expansion of 19.6%, as shown in Table 2), indicating the onset of the solid-solution β branch of the hydride phase. Remarkably, in this sample, there is still a nonhydrogenated intermetallic phase, which may be due to the partial desorption during the sample handling.

For the compounds with a larger Mn content (y = 0.2, 0.3), the PCIs show a "second plateau" (Figure 1). Their XRD patterns show the formation of an intermediate hydride between the intermetallic compounds and the AB_2H_w hydride with a superstructure. The intensity of the Bragg peaks of this intermediate phase became markedly important for y = 0.3 at hydrogen concentrations up to 1.9 H/f.u., indicating that the formation of such a phase occurs more easily for compounds with a larger Mn content and a moderate H concentration. It is also obvious that for Mn0.3, the decrease in peak intensity compared with the background and the broadness of the diffraction peaks with H content may indicate a loss of crystallinity for all phases after hydrogen absorption. For the Mn0.2 and Mn0.3 compounds, the contribution of the bump in the background increases with H content. This shape of the background suggests a partial amorphization of the hydride, as it has been already observed in Ani$_2$ compounds [33]. The second plateau can also be related to a transformation from crystalline to amorphous hydride.

2.2.3. Structural Evolution upon Dehydrogenation

XRD characterization was performed after PCI measurements and subsequent hydrogen desorption under dynamic vacuum at 150 °C (Figure 3) for the single-phase compounds. As shown in Figure 3, a large bump with a maximum of around 2θ = 42° is observed for all samples. After dehydrogenation, the Bragg peaks of the initial $Y_{0.9}Ni_{1.9}Mn_{0.1}$ intermetallic are still present, as well as that of $Y_{0.86}Ni_{1.8}Mn_{0.2}$ but with a smaller intensity. The XRD pattern of desorbed $Y_{0.9}Ni_{1.7}Mn_{0.3}$ hydride displays mainly a broad bump in the background and a few peaks belonging to Y_2O_3 that were already present in the initial alloy. This indicates the full HIA occurrence of this compound, as observed for desorbed $Y_{0.95}Ni_2$ hydride. The presence of broad crystalline diffraction peaks of the $C15$ phase in equilibrium with an amorphous contribution after PCI measurement in the $Y_{0.9}Ni_{1.9}Mn_{0.1}$ compound indicates better structural stability than in other Mn compounds with a partial HIA.

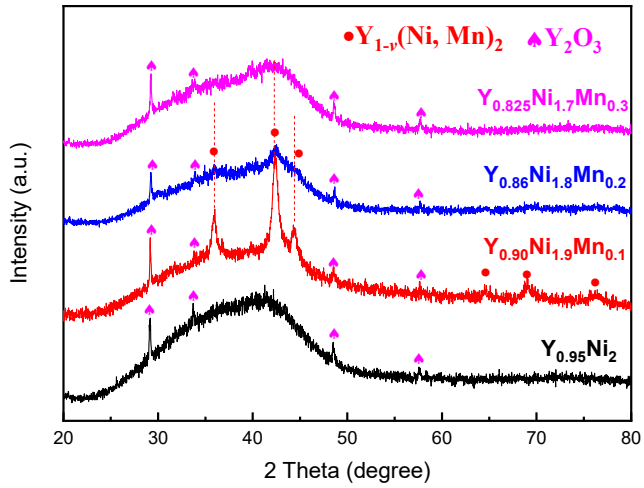

Figure 3. XRD patterns of the compounds with single-phase structures after PCI measurements and hydrogen desorption under primary vacuum at 150 °C.

2.3. TG–DSC Studies of the Amorphous Hydrides

To understand the hydrogen desorption properties of amorphous hydrides, thermal analysis was performed for $Y_xNi_{2-y}Mn_y$ (x = 0.95, 0.90, 0.86, 0.825, y = 0, 0.1, 0.2, 0.3) compounds after hydrogen desorption at 150 °C under primary vacuum. The TG–DSC curves are shown in Figure 4.

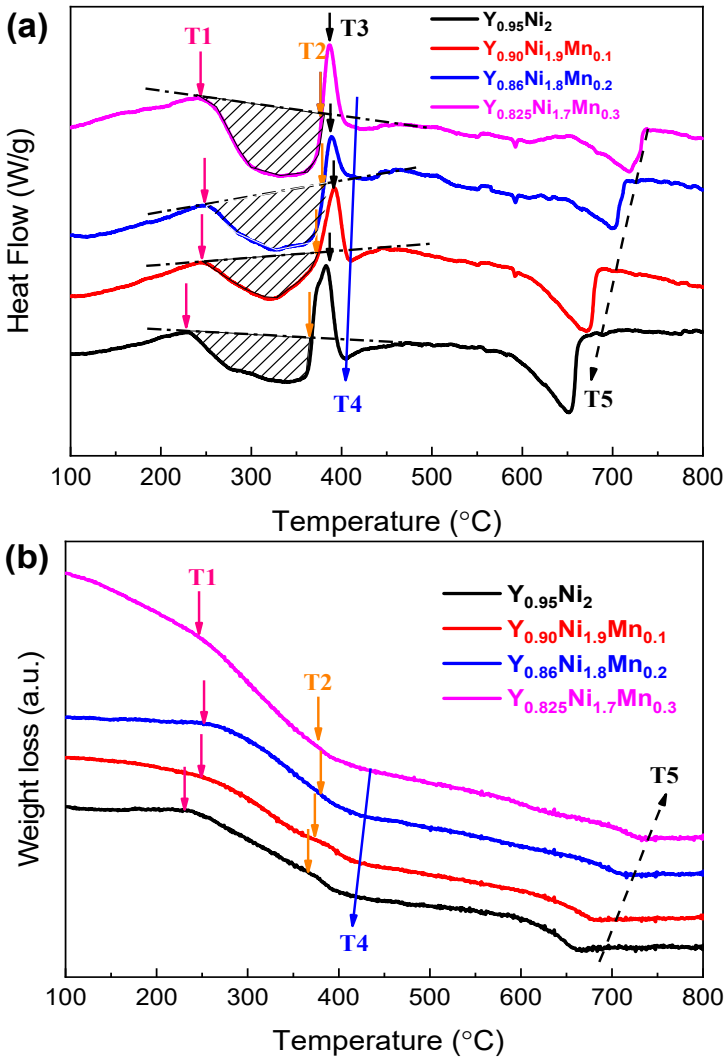

Figure 4. DSC (**a**) and TG (**b**) curves of $Y_xNi_{2-y}Mn_y$ compound (x = 0.95, 0.9, 0.86, 0.825, y = 0, 0.1, 0.2, 0.3) samples upon PCI tests and hydrogen desorption under dynamic vacuum. T1 and T2 are the beginning and end temperatures for hydrogen desorption of amorphous hydrides, T4 is the end temperature of crystallization, and T5 is the end temperature of the second endothermic peak which can correspond to the hydrogen desorption from YH_2.

All the DSC curves of single-phase compounds with either a superstructure or a *C*15 structure show a large broad endothermic peak between T1 and T2, followed by a sharp exothermic peak at T3 (Figure 4a). In the temperature region between T1 and T2, a weight loss is observed in the TG curves. It should correspond to the hydrogen desorption of amorphous hydrides (between T1 and T2) and phase crystallization (T3). The shaded area below the broken line should correspond, therefore, to enthalpy changes during the hydrogen desorption from the amorphous hydrides. This temperature does not vary with the Mn content. On the contrary, the hydrogen desorption content measured by TG increases with the Mn content (Mn0.1 to Mn0.3, Figure 4b). The maximum amount of hydrogen desorption can be observed for Mn0.3, indicating a larger initial amount of amorphous hydrides in the sample, in agreement with previous results (Figure 3). The desorbed H_2 per mol of sample was calculated from the sample weight loss (TG curves). Then, by integrating the endothermic peaks (shadow area on the DSC curves), the enthalpy changes for one mole of released H_2 were calculated. The enthalpy changes are listed in Table 3. The Mn0.1 and Mn0.2 compounds show the minimum and maximum enthalpies, respectively.

Table 3. The hydrogen content released from the amorphous hydride phase (where *a* stands for amorphous, and *w* stands for the remaining hydrogen in the amorphous hydrides) and the enthalpy changes per mol H_2.

Samples	Hydrogen Desorption (mol H_2/mol Sample)	Δ*H* (kJ/mol H_2)
a-$Y_{0.95}Ni_2H_w$	0.39	41.58
a-$Y_{0.90}Ni_{1.9}Mn_{0.1}H_w$	0.34	35.16
a-$Y_{0.86}Ni_{1.8}Mn_{0.2}H_w$	0.39	52.80
a-$Y_{0.825}Ni_{1.7}Mn_{0.3}H_w$	0.59	39.48

Just after hydrogen desorption, the following exothermic peak (shown in Figure 4a) should correspond to the recrystallization of the amorphous phase, T4 being the temperature at which the crystallization ends. At around 650 °C, there is another endothermic peak for all samples with a shift to a higher temperature as the Mn content increases.

To interpret the DSC curves, XRD analysis was carried out for the samples after thermal analysis at temperatures T4 and T5, and then they were cooled down to room temperature. As shown in Figure 5a, after T4, all the XRD patterns contain crystalline AB_3-type Y(Ni, Mn)$_3$ and YH_2 phases, and small amounts of AB_2 and Y_2O_3 are also present. This may indicate that during the hydrogen desorption of the amorphous hydride, a disproportionation reaction occurs; as YH_2 is a very stable hydride, the freshly formed Y catches hydrogen and forms yttrium hydride. As a result of the balance, the crystalized phase is richer in the *B* element forming Y(Ni, Mn)$_3$ instead of Y(Ni, Mn)$_2$. After heating to T5, the absence of the YH_2 phase and the presence of the *C*15 or superstructure Y (Ni, Mn)$_2$ phase indicates a recombination reaction between the YH_2 and AB_3-type Y(Ni, Mn)$_3$ phase (Figure 5b) to form the initial Laves phase compound. This reaction is accompanied by a weight loss due to the hydrogen release from YH_2 (Figure 4b). The increase in T5 with the Mn content reflects the relative stability of the AB_2/AB_3 phase: the larger the Mn content, the more stable the AB_3 phase as observed at room temperature on the alloys. The presence of an Y_2O_3 oxide and the remaining AB_3 phase means an incomplete recombination reaction due to partial oxidation of Y during DSC measurement.

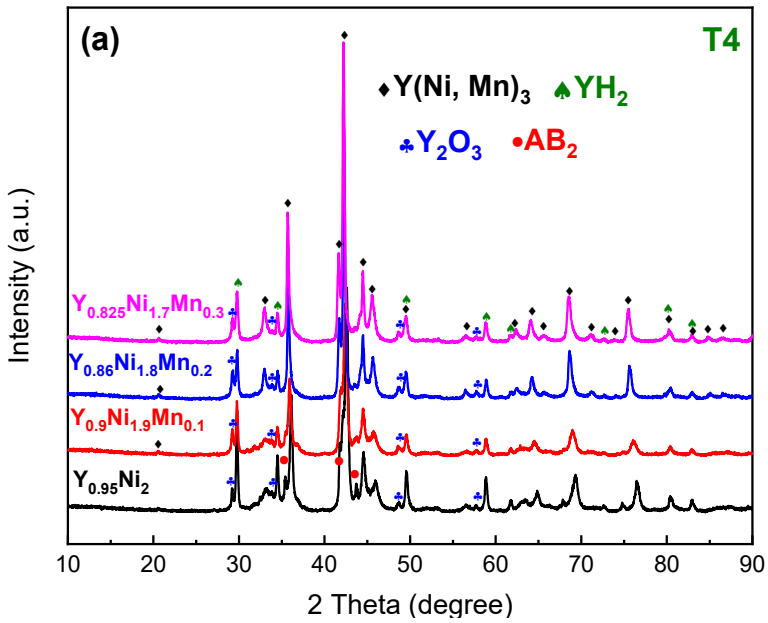

Figure 5. *Cont.*

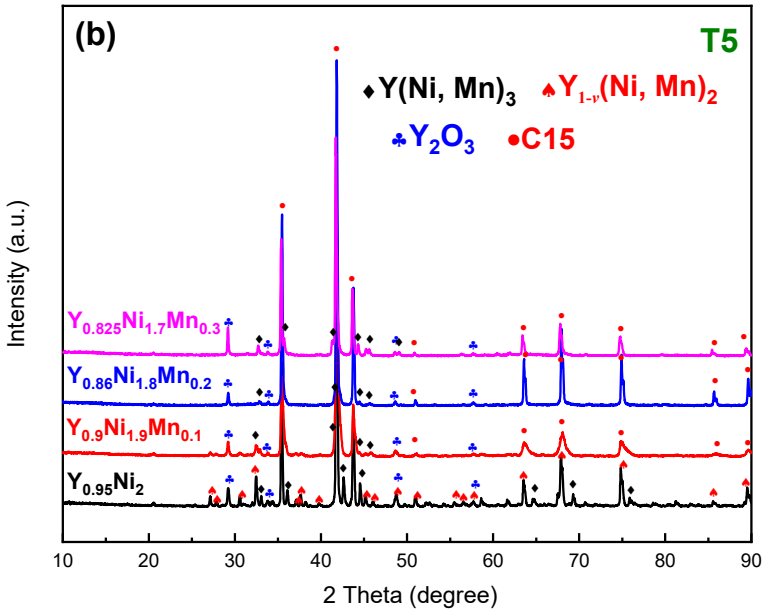

Figure 5. The XRD patterns of $Y_xNi_{2-y}Mn_y$ (x = 0.95, 0.90, 0.86, 0.825, y = 0, 0.1, 0.2, 0.3) compounds upon thermal analysis at different temperatures: T4, the end temperature of crystallization (**a**); T5, the end temperature of the second endothermic peak (**b**).

Similar results have been reported in $CeNi_2$: the recrystallization upon heating of the amorphous $CeNi_{2.16}H_{3.65}$ hydride yields first a mixture of $CeNi_5$ and CeH_x, and then a progressive transformation between $CeNi_5$ and CeH_x towards the $CeNi_2$ intermetallic occurs [34].

3. Discussion

3.1. Mn Substitution Effects on Phase Occurrence and Structures

The binary $Y_{0.95}Ni_2$ compound crystallizes in an earlier reported $TmNi_2$-type superstructure with the space group $F\bar{4}3m$ [29,31,35]. Upon Mn for Ni substitution in $Y_xNi_{2-y}Mn_y$ ($y \geq 0.1$), a structural transformation from a $TmNi_2$-type superstructure to a *C*15 Laves phase structure with disordered Y vacancies occurs. Such structural evolution has been reported in $Y_{0.95}Ni_{2-y}B_y$ (B = Cu, Fe, Al) systems [21,36]. Meanwhile, single-phase compounds with a *C*15 structure can be obtained by adjusting both the Y and Mn contents ($Y_{0.90}Ni_{1.7}Mn_{0.3} \rightarrow Y_{0.825}Ni_{1.7}Mn_{0.3}$, e.g.,). With the Mn content increasing from 0 to 0.3, Y vacancy formation was only observed in $Y_{0.95}Ni_2$ and $Y_{0.90}Ni_{1.9}Mn_{0.1}$ compounds, whereas $Y_{0.86}Ni_{1.8}Mn_{0.2}$ and $Y_{0.825}Ni_{1.7}Mn_{0.3}$ showed Mn occupations in both the Y and Ni sites without vacancy formation [30].

3.2. Hydrogenation Properties

Due to Y vacancy formation or bilateral distribution of Mn atoms, the PCIs of $Y_{0.95}Ni_2$, $Y_{0.86}Ni_{1.8}Mn_{0.2}$, and $Y_{0.825}Ni_{1.7}Mn_{0.3}$ compounds show a similar behavior but are different from that of $Y_{0.90}Ni_{1.9}Mn_{0.1}$ [30]. After a short plateau at low pressure, Mn0.1 shows a sloped branch, whereas the other three compounds show a second plateau (Figure 1b). The change of equilibrium pressures of the first plateau is small for all hydrides up to 1.2 H/f.u. (Figure 1). However, by comparing the XRD patterns of $Y_{0.90}Ni_{1.9}Mn_{0.1}H_2$, $Y_{0.86}Ni_{1.8}Mn_{0.2}H_{2.1}$, and $Y_{0.825}Ni_{1.7}Mn_{0.3}H_{1.9}$, it is clear that for the Mn0.1 compound, no amorphous hydride is formed while a bump in the background for Mn0.2 and Mn0.3 indicates partial amorphization for an H content of around 2 H/f.u. (Figure 2).

Regarding the hydrogen desorption on the PCI, most of the hydrogen cannot be fully released under PCI measurement conditions (Figure 1). The XRD patterns (Figure 3) of samples dehydrogenated under vacuum show that all samples contain amorphous hydrides, indicating hydrogen-induced amorphization (HIA). As reported in other rare-earth-based

AB_2 compounds, the occurrence of HIA depends on the hydrogenation pressure, time, and temperature [37–40]. It was reported that $Y_{0.95}Ni_2$ forms a crystalline hydride at 100 °C under a pressure up to 3 MPa and becomes amorphous under 5 MPa of hydrogen [23]. We have measured the PCI at 150 °C with a maximum pressure of 10 MPa. After hydrogenation at RT up to 2 MPa, a crystalline hydride was still observed, but a disproportion occurred after PCI desorption. We can therefore assume that the amorphization occurs in the solid-solution branch between 2 and 5 MPa for Mn0. For Mn0.2 and Mn0.3 compounds, we interpret that the second plateau (Figure 1b) compounds the HIA, where the crystalline hydride transforms to an amorphous hydride with an increasing hydrogen content.

Another feature of Figure 3 is a partially recovered intermetallic phase for Mn0.1; we can conclude that Mn0.1 shows a better structural stability upon hydrogenation than Mn0, Mn0.2, and Mn0.3 compounds. As shown in a previous work [30], in the Mn0.1 compound, the Mn atoms are substituted only in the Ni site, whereas the vacancies are in the Y site. For compounds with a larger Mn content (Mn0.2 and Mn0.3), the Mn atoms occupy both the Y site and the Ni site, and the number of vacancies in the Y site is reduced [30]. Considering that for Mn0.1 ($Y_{0.90}Ni_{1.9}Mn_{0.1}$), Y vacancies ($r_{\text{vacancy}} = 0$) are in the *A* site, whereas the Ni and Mn atoms are in the *B* site, its average atomic radius ratio $r_A/r_B = 1.29$ is smaller than that for two other Mn compounds where Mn is located in both *A* and *B* sites (1.40 for Mn0.2 and 1.39 for Mn0.3). The larger r_A/r_B ratio for Mn0.2 and Mn0.3 compared with the ideal value of 1.225 and the critical value of 1.37 observed for the onset of HIA can explain their structural stability compared with Mn0.1. This agrees with the observation that the atomic radius ratio is a dominating factor for the HIA in AB_2 Laves phase compounds [39,41]. To reach the ideal atomic radius ratio, the *A* site vacancies and the antisite occupations (Mn occupying the *A* site) should be considered.

However, changes in the electronic structure caused by Mn substitution cannot be fully excluded. It was shown that for AB_2 (*A* = rare earth; *B* = Mn, Fe, Co, and Ni), in the case of the same *A* element, the stability of AB_2 compounds depends on the *B* element; it increases from Mn, Fe, and Co to Ni [42–44], and the geometric effect plays a reverse role.

Here, since Mn has fewer 3*d*-electrons than Ni, Mn occupation in Ni sites will cause a reduction in electron number in the Ni *d*-shell. The literature [45–49] reported that Mn occupation in *C*15-type RNi_2Mn (*R* = Tb, Dy, Ho, and Er) compounds prominently impacts their electronic structures. The calculation of RNi_2Mn indicated an increase in the density of the state at the Fermi level due to electronic transfer [49]. Indeed, the formation of *R*-Ni compounds relies on the charge transfer and filling of the 3*d*-electron band by valence electrons of rare-earth atoms [50]; Mn doping in *R* sites will cause a decrease in *R* atom number. Such changes in the electronic structure may have a direct impact on the structural stability during hydrogen sorption, which deserves further exploration.

Upon thermal analysis, the phase occurrence with increasing temperature can be summarized into three steps as follows (*a*-: amorphous, *c*-: crystalline):

$$a\text{-}Y_{1-v}(\text{Ni, Mn})_2H_w \xrightarrow[\text{1st endothermic}]{} a\text{-}Y_{1-v}(\text{Ni, Mn})_2H_{w'} + H_2 \xrightarrow[\text{endothermic}]{} c\text{-}Y(\text{Ni, Mn})_3 + c\text{-}YH_2 + H_2 \xrightarrow[\text{2nd endothermic}]{} c\text{-}Y_{1-v}(\text{Ni, Mn})_2 + H_2.$$

Considering the better performance in hydrogen sorption of $Y_{0.9}Ni_{1.9}Mn_{0.1}$ than other high Mn-containing compounds, the geometric effect caused by Y vacancies and Mn exclusive occupation in Ni sites is more important. The formation of Y vacancies shifts the surrounding Y atoms closer to the vacancy center [19]; thus, a Y–Y distance is contracted near the vacancy, whereas the other distances are expanded. As a result, the site with a Y vacancy is much smaller than those occupied by Y atoms, and the average $r_{(\text{Y+vacancy})}/r_{(\text{Ni+Mn})}$ ratio becomes close to or smaller than 1.37. Consequently, in Mn0.1, HIA is partially suppressed by the synergistic effect of Y vacancy formation and Mn for Ni substitution. These results may be used to guide the research for more stable Laves phases for hydrogen storage.

4. Materials and Methods

The synthesis of $Y_xNi_{2-y}Mn_y$ ($0.825 \leq x \leq 0.95$, $0.1 \leq y \leq 0.3$) compounds is described in [30]. Pressure–composition isotherm (PCI) curves were measured at 150 °C by an experimental apparatus based on the Sieverts method using 100 µm crushed powder. Before PCI measurements, the samples were activated at 150 °C under vacuum for 1 h. After PCI measurements, a 1 h dynamic vacuum at 150 °C was adopted for hydrogen desorption. Hydrides with different hydrogen concentrations were prepared at room temperature for XRD measurements. The sample holders were opened in the air to favor surface passivation to avoid hydrogen desorption. To observe the structural behaviors during hydrogen desorption and crystallization processes, the dehydrogenated samples were subsequently analyzed by DSC and thermogravimetric analysis (ATG Setsys Evolution 16 SETARAM) with a heating rate of 5 °C/min from 25 to 900 °C under argon flow. XRD measurements were performed after DSC at different temperatures.

XRD measurements of as-cast alloys were carried out with a D8 DAVINCI diffractometer from Bruker with Cu-K_α radiation in the 2θ range of 10°–90°. Diffraction patterns were collected at 40 kV and 40 mA for the anode of the X-ray tube. Rietveld analyses of the experimental data were performed with the program FullProf [51]. The phase compositions were examined by electron probe microanalysis (EPMA) using CAMECA (Gennevillier, France) SX100.

5. Conclusions

The structural and hydrogen sorption behaviors of intermetallic compounds with the nominal composition $Y_xNi_{2-y}Mn_y$ (x = 0.95, 0.90, 0.86, 0.825, y = 0, 0.1, 0.2, 0.3) were investigated systematically. The formation of the *C*15 Laves phase structure with disordered vacancies is favored against the superstructure one of $Y_{0.95}Ni_2$. The single *C*15 phase can be formed in a composition region by adjusting both the Y and Mn components.

Y vacancy formation and Mn occupation in Ni sites (Mn0.1) enhance the structural stability and reduce the HIA effect. Mn occupation in Y sites shows the possibility to further decrease r_A/r_B, but a larger Mn content ($y \geq 0.2$) yields less structural stability during hydrogenation, i.e., an easier tendency towards HIA.

Author Contributions: H.S.: data curation, formal analysis, investigation, writing—original draft, writing—review and editing; V.P.-B.: writing—original draft, writing—review and editing; P.L.: editing; L.J.: funding acquisition, supervision; J.Z.: conceptualization, formal analysis, writing—original draft, writing—review and editing, funding acquisition, supervision. All authors have read and agreed to the published version of the manuscript.

Funding: This work is supported by Campus France under Cai Yuanpei project 44027 WH.

Data Availability Statement: Data will be made available on request.

Conflicts of Interest: The authors declare no conflicts of interest. The funder was not involved in the study design, collection, analysis, interpretation of data, the writing of this article or the decision to submit it for publication.

References

1. Rusman, N.A.A.; Dahari, M. A Review on the Current Progress of Metal Hydrides Material for Solid-State Hydrogen Storage Applications. *Int. J. Hydrogen Energy* **2016**, *41*, 12108–12126. [CrossRef]
2. Liang, F.; Lin, J.; Cheng, Y.; Yin, D.; Wu, Y.; Wang, L. Gaseous Sorption and Electrochemical Properties of Rare-Earth Hydrogen Storage Alloys and Their Representative Applications: A Review of Recent Progress. *Sci. China Technol. Sci.* **2018**, *61*, 1309–1318. [CrossRef]
3. Fang, F.; Chen, Z.; Wu, D.; Liu, H.; Dong, C.; Song, Y.; Sun, D. Subunit Volume Control Mechanism for Dehydrogenation Performance of AB3-Type Superlattice Intermetallics. *J. Power Sources* **2019**, *427*, 145–153. [CrossRef]
4. Denys, R.V.; Yartys, V.A.; Webb, C.J. Hydrogen in $La_2MgNi_9D_{13}$: The Role of Magnesium. *Inorg. Chem.* **2012**, *51*, 4231–4238. [CrossRef] [PubMed]

5. Liu, J.; Han, S.; Li, Y.; Zhao, X.; Yang, S.; Zhao, Y. Cooperative Effects of Sm and Mg on Electrochemical Performance of La-Mg-Ni-Based Alloys with A_2B_7- and A_5B_{19}-Type Super-Stacking Structure. *Int. J. Hydrogen Energy* **2015**, *40*, 1116–1127. [CrossRef]
6. Liu, J.; Li, Y.; Han, D.; Yang, S.; Chen, X.; Zhang, L.; Han, S. Electrochemical Performance and Capacity Degradation Mechanism of Single-Phase La-Mg-Ni-Based Hydrogen Storage Alloys. *J. Power Sources* **2015**, *300*, 77–86. [CrossRef]
7. Ouyang, L.Z.; Cao, Z.J.; Li, L.L.; Wang, H.; Liu, J.W.; Min, D.; Chen, Y.W.; Xiao, F.M.; Tang, R.H.; Zhu, M. Enhanced High-Rate Discharge Properties of $La_{11.3}Mg_{6.0}Sm_{7.4}Ni_{61.0}Co_{7.2}Al_{7.1}$ with Added Graphene Synthesized by Plasma Milling. *Int. J. Hydrogen Energy* **2014**, *39*, 12765–12772. [CrossRef]
8. Kadir, K.; Sakai, T.; Uehara, I. Synthesis and Structure Determination of a New Series of Hydrogen Storage Alloys; RMg_2Ni_9 (*R* = La, Ce, Pr, Nd, Sm and Gd) Built from $MgNi_2$ Laves-Type Layers Alternating with AB_5 Layers. *J. Alloys Compd.* **1997**, *257*, 115–121. [CrossRef]
9. Magee, C.B.; Liu, J.; Lundin, C.E. Relationships between Intermetallic Compound Structure and Hydride Formation. *J. Less Common Met.* **1980**, *78*, 119–138. [CrossRef]
10. Soubeyroux, J.L.; Bououdina, M.; Fruchart, D.; de Rango, P. Phase Stability and Neutron Diffraction Studies of Laves Phases $Zr(Cr_{1-x}M_x)_2$ with M = $(Cu_{0.5}Ni_{0.5})$ and 0 < x < 0.2 and Their Hydrides. *J. Alloys Compd.* **1995**, *231*, 760–765. [CrossRef]
11. Soubeyroux, J.L.; Fruchart, D.; Biris, A.S. Structural Studies of Laves Phases $ZrCo(V_{1-x}Cr_x)$ with $0 \leq x \leq 1$ and Their Hydrides. *J. Alloys Compd.* **1999**, *293–295*, 88–92. [CrossRef]
12. Suzuki, A.; Nishimiya, N.; Ono, S. Thermodynamic Properties of $Zr(Fe_xMn_{1-x})_2$-H_2 Systems. *J. Less Common Met.* **1983**, *89*, 263–268. [CrossRef]
13. Wijayanti, I.D.; Denys, R.; Volodin, A.A.; Lototskyy, M.V.; Guzik, M.N.; Nei, J.; Young, K.; Roven, H.J.; Yartys, V. Hydrides of Laves Type Ti–Zr Alloys with Enhanced H Storage Capacity as Advanced Metal Hydride Battery Anodes. *J. Alloys Compd.* **2020**, *828*, 154354. [CrossRef]
14. Zhang, X.; Li, B.; Wang, L.; Xiong, W.; Li, J.; Zhou, S.; Xu, J.; Zhao, Y.; He, X.; Yan, H. Hydrogen Storage Properties of AB_2 Type Ti–Zr–Cr–Mn–Fe Based Alloys. *Int. J. Hydrogen Energy* **2024**, *51*, 193–201. [CrossRef]
15. Kandavel, M.; Bhat, V.V.; Rougier, A.; Aymard, L.; Nazri, G.-A.; Tarascon, J.-M. Improvement of Hydrogen Storage Properties of the AB_2 Laves Phase Alloys for Automotive Application. *Int. J. Hydrogen Energy* **2008**, *33*, 3754–3761. [CrossRef]
16. Aoki, K.; Li, H.-W.; Dilixiati, M.; Ishikawa, K. Formation of Crystalline and Amorphous Hydrides by Hydrogenation of C15 Laves Phase YFe_2. *Mater. Sci. Eng. A* **2007**, *449–451*, 2–6. [CrossRef]
17. Shen, H.; Zhang, J.; Paul-Boncour, V.; Li, P.; Li, Z.; Wu, Y.; Jiang, L. AB_2-Type Rare Earth-Based Compounds with C-15 Structure: Looking for Reversible Hydrogen Storage Materials. *J. Rare Earths* 2023, in press. [CrossRef]
18. Latroche, M.; Paul-Boncour, V.; Percheron-Guegan, A. Structural Instability in $R_{1-x}Ni_2$ Compounds and Their Hydrides (R = Y, Rare Earth). *Z. Für Phys. Chem.* **1993**, *179*, 261–268. [CrossRef]
19. Paul-Boncour, V.; Lindbaum, A.; Latroche, M.; Heathman, S. Homogeneity Range and Order–Disorder Transitions in $R_{1-x}Ni_2$ Laves Phase Compounds. *Intermetallics* **2006**, *14*, 483–490. [CrossRef]
20. Shen, H.; Paul-Boncour, V.; Latroche, M.; Cuevas, F.; Li, P.; Yuan, H.; Li, Z.; Zhang, J.; Jiang, L. Investigation of the Phase Occurrence and H Sorption Properties in the $Y_{33.33}Ni_{66.67-x}Al_x$($0 \leq x \leq 33.33$) System. *J. Alloys Compd.* **2021**, *888*, 161375. [CrossRef]
21. Paul-Boncour, V.; Percheron-Guegan, A.; Diaf, M.; Achard, J.C. Structural Characterization of RNi2 (R ≡ La, Ce) Intermetallic Compounds and Their Hydrides. *J. Less Common Met.* **1987**, *131*, 201–208. [CrossRef]
22. Zhao, S.; Wang, H.; Liu, J. Exploring the Hydrogen-Induced Amorphization and Hydrogen Storage Reversibility of $Y(Sc)_{0.95}Ni_2$ Laves Phase Compounds. *Materials* **2021**, *14*, 276. [CrossRef]
23. Przewoznik, J.; Paul-Boncour, V.; Latroche, M.; Percheron-Guégan, A. Structural Study of YMn_2 Hydrides. *J. Alloys Compd.* **1995**, *225*, 436–439. [CrossRef]
24. Figiel, H.; Przewoznik, J.; Paul-Boncour, V.; Lindbaum, A.; Gratz, E.; Latroche, M.; Escorne, M.; Percheron-Guégan, A.; Mietniowski, P. Hydrogen Induced Phase Transitions in YMn_2. *J. Alloys Compd.* **1998**, *274*, 29–37. [CrossRef]
25. Latroche, M.; Paul-Boncour, V.; Percheron-Guégan, A.; Bourée-Vigneron, F. Temperature Dependence Study of $YMn_2D_{4.5}$ by Means of Neutron Powder Diffraction. *J. Alloys Compd.* **1998**, *274*, 59–64. [CrossRef]
26. Paul-Boncour, V.; Filipek, S.M.; Dorogova, M.; Bourée, F.; André, G.; Marchuk, I.; Percheron-Guégan, A.; Liu, R.S. Neutron Diffraction Study, Magnetic Properties and Thermal Stability of YMn_2D_6 Synthesized under High Deuterium Pressure. *J. Solid State Chem.* **2005**, *178*, 356–362. [CrossRef]
27. Matsuo, M.; Miwa, K.; Semboshi, S.; Li, H.-W.; Kano, M.; Orimo, S. First-Principles Studies of Complex Hydride YMn_2H_6 and Its Synthesis from Metal Hydride $YMn_2H_{4.5}$. *Appl. Phys. Lett.* **2011**, *98*, 221908. [CrossRef]
28. Suwarno, S.; Dicky, G.; Suyuthi, A.; Effendi, M.; Witantyo, W.; Noerochim, L.; Ismail, M. Machine Learning Analysis of Alloying Element Effects on Hydrogen Storage Properties of AB_2 Metal Hydrides. *Int. J. Hydrogen Energy* **2022**, *47*, 11938–11947. [CrossRef]
29. Latroche, M.; Paul-Boncour, V.; Percheron-Guégan, A.; Achard, J.C. Structure Determination of $Y_{0.95}Ni_2$ by X-Ray Powder Diffraction. *J. Less Common Met.* **1990**, *161*, L27–L31. [CrossRef]
30. Shen, H.; Setayandeh, S.S.; Paul-Boncour, V.; Emery, N.; Li, Z.; Li, P.; Yuan, H.; Jiang, L.; Burr, P.A.; Latroche, M.; et al. Experimental and Computational Study on the C15 Phase Structure Stability of $Y_zNi_{2-y}Mn_y$ System. *J. Alloys Compd.* **2023**, *952*, 169632. [CrossRef]

31. Percheron-Guégan, A.; Paul-Boncour, V.; Latroche, M.; Achard, J.C.; Bourée-Vigneron, F. Structure of $Y_{0.95}Ni_2$ and Its Hydride. *J. Less Common Met.* **1991**, *172–174*, 198–205. [CrossRef]
32. Nakhl, M.; Bobet, J.L.; Chevalier, B.; Darriet, B. Hydrogen Sorption Properties of Composites Mixtures Mg+YNi Submitted to Mechanical Grinding. *J. Metastable Nanocrystalline Mater.* **2001**, *10*, 637–642. [CrossRef]
33. Aoki, K.; Yamamoto, T.; Masumoto, T. Hydrogen Induced Amorphization in RNi_2 Laves Phases. *Scr. Metall.* **1987**, *21*, 27–31. [CrossRef]
34. Paul-Boncour, V.; Lartigue, C.; Percheron-Guégan, A.; Achard, J.C.; Pannetier, J. In Situ Neutron Powder Diffraction Measurements of the Absorption and Desorption of Hydrogen (Deuterium) in (La,Ce)Ni_2 Compounds: Amorphization and Recrystallization. *J. Less Common Met.* **1988**, *143*, 301–313. [CrossRef]
35. Deutz, A.F.; Helmholdt, R.B.; Moleman, A.C.; De Mooij, D.B.; Buschow, K.H.J. Superstructure in the Intermetallic Compound $TmNi_2$. *J. Less Common Met.* **1989**, *153*, 259–266. [CrossRef]
36. Myakush, O.; Babizhetskyy, V.; Myronenko, P.; Michor, H.; Kotur, B.; Bauer, E. Influence of Doping Elements (Cu and Fe) on the Crystal Structure and Electrical Resistivity of YNi_3 and $Y_{0.95}Ni_2$. *Chem. Met. Alloys* **2011**, *4*, 152–159. [CrossRef]
37. Dilixiati, M.; Kanda, K.; Ishikawa, K.; Suzuki, K.; Aoki, K. Thermal Analysis of Hydrogen-Induced Amorphization in C15 Laves RFe_2 Compounds. *J. Alloys Compd.* **2002**, *330–332*, 743–746. [CrossRef]
38. Aoki, K.; Dilixiati, M.; Ishikawa, K. Hydrogen-Induced Transformations in C15 Laves Phases $CeFe_2$ and $TbFe_2$ Studied by Pressure Calorimetry up to 5 MPa. *J. Alloys Compd.* **2003**, *356–357*, 664–668. [CrossRef]
39. Aoki, K.; Li, H.-W.; Ishikawa, K. Process and Mechanism of Hydrogen-Induced Amorphization in C15 Laves Phases RFe_2. *J. Alloys Compd.* **2005**, *404–406*, 559–564. [CrossRef]
40. Aoki, K.; Masumoto, T. Hydrogen-Induced Amorphization of Intermetallics. *J. Alloys Compd.* **1995**, *231*, 20–28. [CrossRef]
41. Aoki, K.; Li, X.-G.; Masumoto, T. Factors Controlling Hydrogen-Induced Amorphization of C15 Laves Compounds. *Acta Metall. Et Mater.* **1992**, *40*, 1717–1726. [CrossRef]
42. Buschow, K.H.J. Intermetallic Compounds of Rare-Earth and 3d Transition Metals. *Rep. Prog. Phys.* **1977**, *40*, 1179–1256. [CrossRef]
43. Zhu, J.H.; Liu, C.T.; Pike, L.M.; Liaw, P.K. Enthalpies of Formation of Binary Laves Phases. *Intermetallics* **2002**, *10*, 579–595. [CrossRef]
44. Zhu, J.H.; Liu, C.T.; Pike, L.M.; Liaw, P.K. A Thermodynamic Interpretation of the Size-Ratio Limits for Laves Phase Formation. *Met. Mat Trans A* **1999**, *30*, 1449–1452. [CrossRef]
45. Wang, J.L.; Marquina, C.; Ibarra, M.R.; Wu, G.H. Structure and Magnetic Properties of RNi_2Mn Compounds (*R* = Tb, Dy, Ho, and Er). *Phys. Rev. B* **2006**, *73*, 094436. [CrossRef]
46. Mushnikov, N.V.; Gaviko, V.S.; Park, J.; Pirogov, A.N. Crystal and Magnetic Structure of $TbNi_2Mn$. *Phys. Rev. B* **2009**, *79*, 184419. [CrossRef]
47. Mushnikov, N.V.; Gaviko, V.S.; Gerasimov, E.G.; Terentyev, P.B.; Tkach, I.A.; Korolyov, A.V. Magnetic Properties of Non-Stoichiometric RNi_2Mn_x (*R* = Tb, Dy) Compounds. *Solid State Phenom.* **2010**, *168–169*, 200–203. [CrossRef]
48. Gerasimov, E.G.; Mushnikov, N.V.; Terentev, P.B.; Gaviko, V.S.; Inishev, A.A. Magnetic Properties of the Off-Stoichiometric $GdNi_2Mn_x$ Alloys. *J. Alloys Compd.* **2013**, *571*, 132–137. [CrossRef]
49. Korotin, M.A.; Skorikov, N.A.; Efremov, A.V.; Shorikov, A.O. Influence of the Rare-Earth Site Nonstoichiometry and Mn Doping on the Electronic Structure of $TbNi_2$. *J. Magn. Magn. Mater.* **2016**, *397*, 115–119. [CrossRef]
50. Eyring, L.; Gschneidner, K.A. *Handbook on the Physics and Chemistry of Rare Earths*; North-Holland Sole Distributors for the U.S.A. and Canada; Elsevier North-Holland: Amsterdam, The Netherlands; New York, NY, USA, 1978; ISBN 978-0-444-50472-2.
51. Rodríguez-Carvajal, J. Recent Advances in Magnetic Structure Determination by Neutron Powder Diffraction. *Phys. B Condens. Matter* **1993**, *192*, 55–69. [CrossRef]